

Approximate label symmetries improve data scaling

Scott Y. H. Kim,¹ Mathis Lechaume-Robert,^{2,3} and O. Anatole von Lilienfeld^{1,3,4,5,6,*}

¹*Department of Chemistry, Chemical Physics Theory Group,*

University of Toronto, St. George Campus, Toronto, ON M5R 0A3, Canada

²*Institut Courtois, Université de Montréal, Montréal, QC H2V 0B3, Canada*

³*Acceleration Consortium, University of Toronto, Toronto, ON M5R 0A3, Canada*

⁴*Department of Materials Science and Engineering, University of Toronto,
St. George Campus, Toronto, ON M5R 0A3, Canada*

⁵*Department of Physics, University of Toronto, St. George Campus, Toronto, ON M5R 0A3, Canada*

⁶*Vector Institute for Artificial Intelligence, Toronto, ON M5S 1M1, Canada*

(Dated: May 28, 2026)

Enforcing *universal* symmetries in machine learning (ML) models is a common strategy to mitigate data scarcity. We show that exploiting exact, as well as approximate, *label* symmetries can benefit scaling laws. We illustrate the idea for the *s, p, d* orbital densities of the electron in the hydrogen atom, for the three vibrational normal modes of the water molecule, as well as its full 3D potential energy hypersurface. Resulting ML models of electron density and potential energies exhibit superior learning curves, demonstrating improved generalization efficiency. When label symmetries are not exact, the same principles govern the observed learning behavior — up to the convergence floors set by the degree to which the symmetry is approximate. For convex wells in the molecular potential energy surface, a Hessian-based correction suppresses the leading symmetry-breaking error in augmented labels.

I. INTRODUCTION

Machine learning (ML) models trained on QM reference data deliver accurate property predictions at a fraction of first-principles cost [1–3]. Despite the success of fragment-based ('amons') methods or large foundation models [4, 5], their fundamentally interpolative nature makes them unreliable for out-of-distribution queries [6]. Because high-fidelity QM labels are expensive at the scale required for reliable explorations of chemical spaces, inductive biases that increase training data efficiency remain essential.

Symmetry is among the most powerful ways to improve data efficiency. The energy and other observables of an isolated molecule are invariant under $SE(3)$ and permutations of identical nuclei, which the field has exploited at the level of internal coordinate representations [1, 7–12] or through equivariant message-passing architectures [13–18]. Augmenting training data with symmetry-related configurations is a closely related strategy with a long history in computer vision and natural language processing [19–22], though it has seen comparatively little adoption in data-driven models for physics. Empirically, better representations result in a constant factor improvement in data efficiency, while architectural enforcement of $SE(3)$ equivariance has been observed to accelerate the learning rate itself [17, 23].

$SE(3)$ invariance is a universal symmetry of the molecular Hamiltonian and holds for every observable automatically. (Approximate) label symmetries, as we use the term here, are additional invariances of the specific target

function $f(g \cdot x) = f(x)$ that do not follow from those universal symmetries. They relate configurations that can not be connected by global translation, rotation, or index permutation, but nonetheless are approximately degenerate. Not all molecular properties carry such symmetry, and identifying one typically requires prior knowledge of the qualitative functional form of the target itself.

In practice, perfect label symmetries are rare. Analogous to perturbation theory, a candidate symmetry may hold in an idealized limit but be lifted by higher-order corrections. Enforcing exact symmetry constraints when the symmetry is only approximate introduces a bias that no model can remove. This differs from approximate symmetrization currently used in the literature [24–26], where the target is exactly symmetric and the model enforces it only approximately. Here the target itself is not exactly invariant, so even a perfect model reproduces the symmetry breaking because it belongs to the target, rather than the model.

We illustrate this framework for two basic problems in physical chemistry. For exact label symmetries, we use hydrogen atomic orbital densities, which admit discrete (\mathbb{Z}_2) and continuous ($O(3)$) label symmetries. We confirm the learning-curve predictions of exact-symmetry theory [27, 28]. For approximate label symmetries, we focus on reflection symmetry of the molecular potential energy surface about an equilibrium geometry. We show that the asymptotic error floor introduced by the approximate symmetry is governed by the higher odd-order force constants of the target. Building on this result, we introduce a corrected augmentation scheme Aug₃ that uses the molecular Hessian to suppress the leading-order floor at no additional electronic structure cost.

* anatole.vonlilienfeld@utoronto.ca

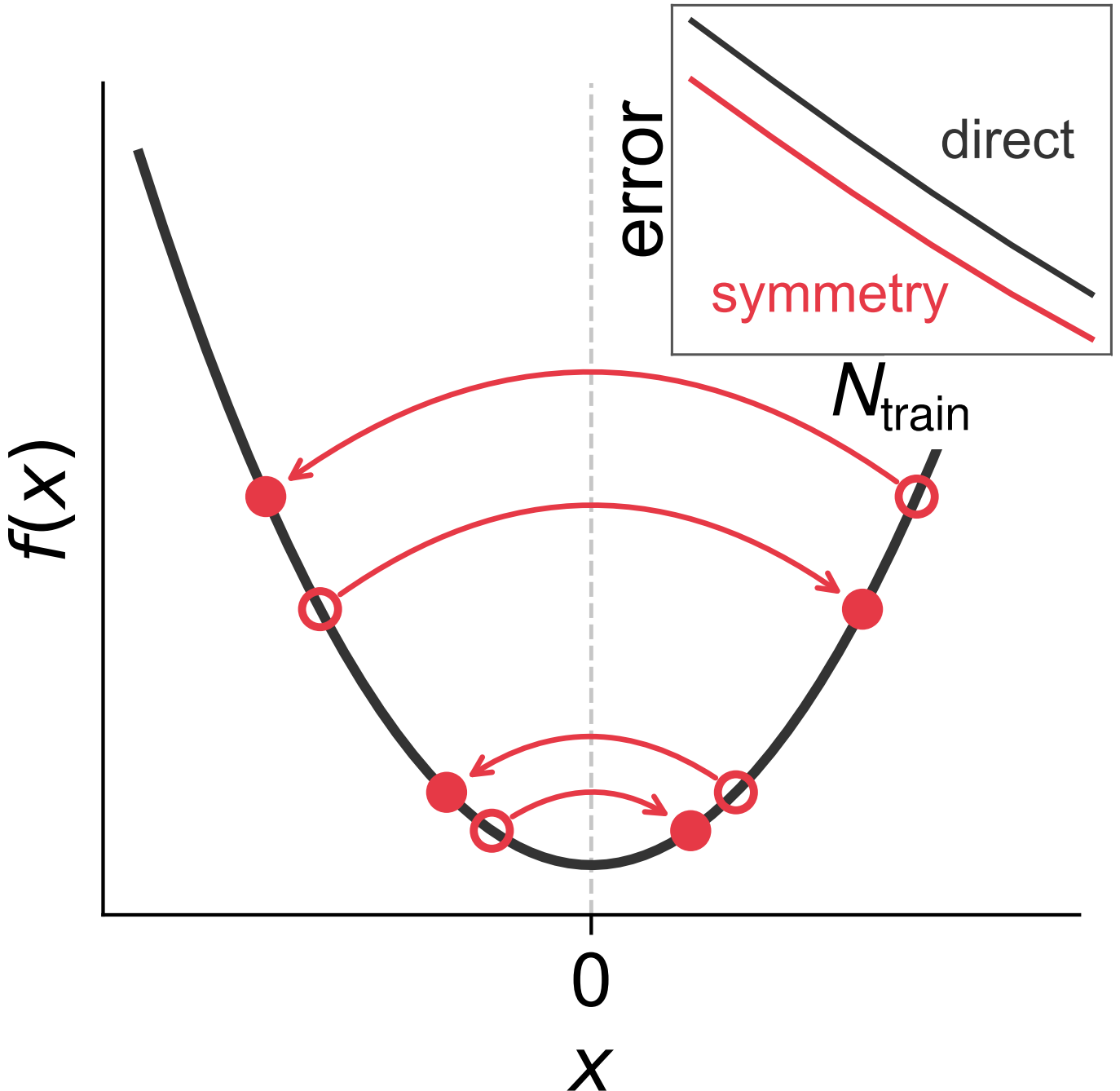


FIG. 1. Schematic illustration of label-symmetry enforcement for data augmentation resulting in improved ML model performance. For an even target function $f(x)$, each input x_i (hollow markers) is related to $-x_i$ (filled markers) by the reflection group \mathbb{Z}_2 and approximately carries the same label. Reflection identifies symmetry-related points and can be used to augment the training dataset. The inset shows the qualitative effect of symmetry on the learning curve. The model trained with all empty and filled points exhibits a constant-factor improvement in performance without a change in learning rate.

II. THEORY AND METHODS

A. Kernel Ridge Regression

With large data budgets, deep learning methods achieve competitive performance without explicit symmetry enforcement. Kernel ridge regression (KRR) [29],

by contrast, excels in the small and moderate training set regimes where label augmentation is most beneficial. In KRR, the prediction for a query point x_q is

$$y_q = \sum_{i=1}^N \alpha_i k(x_i, x_q), \quad (1)$$

with regression coefficients

$$\boldsymbol{\alpha} = (\mathbf{K} + \lambda \mathbf{I})^{-1} \mathbf{y}, \quad (2)$$

where $\mathbf{K}_{ij} = k(x_i, x_j)$, $\lambda > 0$ is the regularization parameter, and \mathbf{y} is the vector of training labels.

B. Enforcing Symmetry in ML Models

Let G be a finite or compact group acting on the input space \mathcal{X} via $x \mapsto g \cdot x$. A target function $f^* : \mathcal{X} \rightarrow \mathbb{R}$ is G -invariant if

$$f^*(g \cdot x) = f^*(x) \quad \forall g \in G, x \in \mathcal{X}. \quad (3)$$

Points related by G form orbits, and enforcing symmetry amounts to constructing a predictor f that is constant on each orbit, $f(g \cdot x) = f(x)$.

1. Data Augmentation

The most naive approach, applicable to finite groups, is to augment the training set with symmetry-related inputs carrying the same label:

$$\{(x_i, y_i)\}_{i=1}^N \longrightarrow \{(g \cdot x_i, y_i) : g \in G, i = 1, \dots, N\}. \quad (4)$$

For exact symmetries, this explicitly ties together all points on each orbit in the empirical risk; exact invariance of the predictor additionally requires assumptions on the model class and training procedure.

2. Input Transformation

A more structured approach is to replace x by a symmetry-adapted representation $M(x)$ that is G -invariant by Eq. 3. Learning f^* on $M(x)$ is equivalent to learning on an invariant subspace of x , which eliminates redundant degrees of freedom. In practice, $M(x)$ may be implemented as a canonicalization to a fundamental domain or as an invariant descriptor coordinate [1, 7–12].

Input transformation and augmentation with the full orbit yield equivalent invariant predictors under the same uniqueness and model-compatibility assumptions.

C. Learning Curves

Learning curves plot prediction error ϵ against training set size N and are the standard data-efficiency benchmark for ML models in quantum chemistry and materials science [1, 3, 12, 30]. Multiple theoretical frameworks have consistently predicted an inverse power-law decay of ϵ with N [31–41], confirmed empirically in many settings using neural networks [42] and kernel methods [43, 44].

We therefore model the learning curve by

$$\epsilon(N) - \epsilon_\infty \approx AN^{-\beta}, \quad (5)$$

where $\epsilon_\infty = \lim_{N \rightarrow \infty} \epsilon(N)$ is the asymptotic error floor, A is a prefactor, and β is the power-law exponent. For deterministic, exactly labeled data $\epsilon_\infty = 0$; inconsistent or noisy labels raise it to a positive value that additional data cannot reduce [45, 46]. In the approximate-symmetry setting studied below, augmenting with mirror points assigns deterministically incorrect labels, producing a nonzero ϵ_∞ even without stochastic noise.

Symmetry acts on A and β through different mechanisms depending on whether the group is continuous or discrete. For continuous symmetries, a G -invariant function depends only on the orbit of its input under G , reducing the effective dimensionality of the learning problem. Since learning rates for smooth functions improve with lower effective dimension [28], continuous symmetry increases β rather than only the prefactor A ; higher levels of $SE(3)$ equivariance yield systematically steeper learning curves empirically [17, 23].

By contrast, enforcing invariance under a finite group G effectively augments each training point with its $|G| - 1$ orbit images, so a model trained on N symmetrized points has access to the information in $|G|N$ unsymmetrized ones, provided no two training points are G -related. In the power-law regime where ϵ_∞ is negligible,

$$\ln \epsilon(|G|N) = \ln A - \beta \ln |G| - \beta \ln N, \quad (6)$$

and comparison to the unsymmetrized model gives

$$\ln \left(\frac{\epsilon(|G|N)}{\epsilon(N)} \right) = -\beta \ln |G|, \quad (7)$$

a constant independent of N , so discrete symmetry acts as a pure horizontal shift by $\ln |G|$ on a log-log plot. Equation (7) holds only in the pre-floor regime; ϵ_∞ for each augmentation scheme is derived in the following section from a Taylor expansion of the approximate mirror labels.

D. Parity and mirror-label errors

In the one-dimensional mode-scan experiments, the relevant symmetry group is the reflection $G = \mathbb{Z}_2$ acting as $q \mapsto -q$, where q is a mass-weighted normal-mode displacement about equilibrium. The electronic energy E in terms of q is

$$E(q) = E(0) + \frac{1}{2}q^2 \partial_q^2 E_0 + \frac{1}{6}q^3 \partial_q^3 E_0 + \frac{1}{24}q^4 \partial_q^4 E_0 + \mathcal{O}(q^5), \quad (8)$$

where $\partial_q^n E_0 = \left(\frac{\partial^n E}{\partial q^n} \right) \Big|_{q=0}$. In a standard frequency analysis, $\partial_q^2 E_0$ is available as the force constant of the vibrational mode. Moving forward, we will denote $E_{\text{HO}}(q) =$

$E(0) + \frac{1}{2}q^2\partial_q^2 E_0$. The energy of the reflected point $-q$ is

$$E(-q) = E_{\text{HO}}(q) - \frac{1}{6}q^3\partial_q^3 E_0 + \frac{1}{24}q^4\partial_q^4 E_0 + \mathcal{O}(q^5), \quad (9)$$

differing only in sign in the cubic term.

With the knowledge that the electronic energy is approximately \mathbb{Z}_2 symmetric about the equilibrium geometry, each training point $(q_i, E(q_i))$ is paired with a mirror point at $-q_i$ carrying the same label

$$\tilde{E}^{\text{sym}}(-q_i) = E(q_i). \quad (10)$$

The error of this approximately symmetric label is

$$\tilde{E}^{\text{sym}}(-q_i) - E(-q_i) = \frac{1}{3}q_i^3\partial_q^3 E_0 + \mathcal{O}(q_i^5). \quad (11)$$

The learned function is even by construction and introduces an irreducible error floor dominated by the cubic term in the expansion.

Another estimate for $E(-q_i)$ that incorporates a correction is obtained by

$$E(q_i) + E(-q_i) = 2E_{\text{HO}}(q_i) + \frac{1}{12}q_i^4\partial_q^4 E_0 + \mathcal{O}(q_i^6) \quad (12)$$

$$\begin{aligned} E(-q_i) &= 2E_{\text{HO}}(q_i) - E(q_i) \quad (13) \\ &+ \frac{1}{12}q_i^4\partial_q^4 E_0 + \mathcal{O}(q_i^6). \end{aligned}$$

Setting

$$\tilde{E}^{\text{corr}}(-q_i) = 2E_{\text{HO}}(q_i) - E(q_i), \quad (14)$$

we obtain a corrected label whose leading error is fourth order:

$$\tilde{E}^{\text{corr}}(-q_i) - E(-q_i) = -\frac{1}{12}q_i^4\partial_q^4 E_0 + \mathcal{O}(q_i^6), \quad (15)$$

Equation (14) has the structure of a single position-Verlet step [47], using q_i as coordinate instead of time. This augmentation scheme is a special case where the first-order term is already 0 by virtue of using a stationary point as reference.

These label errors determine the irreducible convergence floors. In the $N \rightarrow \infty$ limit, every point q is labelled with the true label $E(q)$ as well as an augmented label from the mirror of the point at $-q$. For symmetric augmentation (Aug₂), the augmented label is $\tilde{E}^{\text{sym}}(q) = E(-q)$. The squared-loss minimizer over both labels at q is their average

$$\hat{f}^{\text{sym}}(q) = \frac{E(q) + E(-q)}{2}, \quad (16)$$

the definition of the even component of the function. The irreducible floor in symmetric augmentation must then be the odd component of $E(q)$, which to leading order in the Taylor expansion is

$$\epsilon_{\infty}^{\text{sym}} \approx \frac{1}{6}|\partial_q^3 E_0| \langle |q^3| \rangle, \quad (17)$$

where angle brackets denote the average over the test distribution. For the corrected scheme (Aug₃), the mirror of the point at $-q$ contributes the corrected label $\tilde{E}^{\text{corr}}(q) = 2E_{\text{HO}}(q) - E(-q)$. The average of this label and the true label $E(q)$ is

$$\hat{f}^{\text{corr}}(q) = E_{\text{HO}}(q) + \frac{E(q) - E(-q)}{2}, \quad (18)$$

which contains the harmonic baseline and the odd component of the anharmonic residual. The irreducible floor is determined by the even component of the residual, which to leading order is

$$\epsilon_{\infty}^{\text{corr}} \approx \frac{1}{24}|\partial_q^4 E_0| \langle |q^4| \rangle, \quad (19)$$

a floor that is generically smaller than Eq. (17).

The construction generalizes to d normal-mode coordinates. Writing $\mathbf{q}_i = (q_{i,1}, \dots, q_{i,d})$, the harmonic reference

$$E_{\text{HO}}(\mathbf{q}) = E(0) + \frac{1}{2} \sum_j k_j q_j^2 \quad (20)$$

is invariant under $\mathbf{q} \mapsto -\mathbf{q}$, where diagonality of the harmonic term holds by construction in the normal-mode eigenbasis. Extending Eq. (8), odd-order cross-terms change sign under inversion while even-order terms do not, giving

$$\begin{aligned} E(-\mathbf{q}) &= E_{\text{HO}}(\mathbf{q}) - \frac{1}{6} \sum_{k,l,m} q_k q_l q_m \frac{\partial^3 E}{\partial q_k \partial q_l \partial q_m} \Big|_0 \\ &+ \frac{1}{24} \sum_{k,l,m,n} q_k q_l q_m q_n \frac{\partial^4 E}{\partial q_k \partial q_l \partial q_m \partial q_n} \Big|_0 + \mathcal{O}(q^5). \end{aligned} \quad (21)$$

The symmetric mirror label $\tilde{E}^{\text{sym}}(-\mathbf{q}_i) = E(\mathbf{q}_i)$ has error

$$\begin{aligned} \tilde{E}^{\text{sym}}(-\mathbf{q}_i) - E(-\mathbf{q}_i) &= \frac{1}{3} \sum_{k,l,m} q_{i,k} q_{i,l} q_{i,m} \frac{\partial^3 E}{\partial q_k \partial q_l \partial q_m} \Big|_0 \\ &+ \mathcal{O}(q_i^5), \end{aligned} \quad (22)$$

the multidimensional analogue of Eq. (11). Since $E(\mathbf{q}_i) + E(-\mathbf{q}_i)$ cancels all odd-order terms, the corrected mirror label $\tilde{E}^{\text{corr}}(-\mathbf{q}_i) = 2E_{\text{HO}}(\mathbf{q}_i) - E(\mathbf{q}_i)$ gives

$$\begin{aligned} \tilde{E}^{\text{corr}}(-\mathbf{q}_i) - E(-\mathbf{q}_i) &= -\frac{1}{12} \sum_{k,l,m,n} q_{i,k} q_{i,l} q_{i,m} q_{i,n} \\ &\times \frac{\partial^4 E}{\partial q_k \partial q_l \partial q_m \partial q_n} \Big|_0 \\ &+ \mathcal{O}(q_i^6), \end{aligned} \quad (23)$$

the analogue of Eq. (15). Both errors retain the same cubic/quartic structure as in one dimension but are generally larger in magnitude due to the inclusion of cross-mode coupling.

E. Computational Details

Software

All energy and Hessian calculations of water were performed using the PySCF 2.8.0 package[48] at the ω B97X-D3/def2-TZVPP level of theory[49–51]. All machine learning models were implemented in Python using the QML2 machine learning package[52].

Kernel functions and representations

The hydrogen atom and water 1D experiments use the Laplacian kernel

$$k(x, x') = \exp\left(-\frac{\|x - x'\|_1}{\sigma}\right), \quad (24)$$

where σ is the length-scale hyperparameter. The water 3D experiments use the Gaussian kernel

$$k(x, x') = \exp\left(-\frac{\|x - x'\|_2^2}{2\sigma^2}\right) \quad (25)$$

for the \mathbf{Q} representation, and the screened atomic Gaussian kernel

$$k(\mathbf{X}_I, \mathbf{X}_J) = \sum_{a \in I} \sum_{b \in J} \delta_{Z_a Z_b} \exp\left(-\frac{\|\mathbf{X}_{Ia} - \mathbf{X}_{Jb}\|_2^2}{2\sigma^2}\right) \quad (26)$$

for cMBDF [53, 54], where $\delta_{Z_a Z_b}$ restricts to same-element pairs.

Hyperparameters

For all experiments, hyperparameters were selected by 4-fold cross-validation on a logarithmically spaced sparse grid: $\lambda \in [10^{-14}, 10^{-6}]$ with 5 values. For the s -orbital experiments, the length-scale grid was $\sigma \in [10^{-3}, 10^3]$ with 10 values. For the p_z and d_{xz} experiments, the grid was calibrated to the pairwise distance distribution of each feature set, giving $\sigma \in [10^{-1.5}, 10^{0.5}]$ with 8 values. For the water experiments, $\sigma \in [10^{-2}, 10^2]$ with 15 values.

Water datasets

Vibrational normal modes and force constants were obtained from a frequency analysis at the ω B97X-D3/def2-TZVPP level of theory. For the 1D scans, 1000 geometries along each normal mode were generated by drawing displacements uniformly from $[-q_{\max,j}, q_{\max,j}]$, where $q_{\max,j} = \sqrt{k_B T / k_j}$ is the classical turning point

at $T = 1500$ K. For the 3D dataset, 5000 structures were generated by simultaneous displacement along all three normal-mode coordinates $\mathbf{Q} = (q_1, q_2, q_3)$, with each q_j drawn independently from a Gaussian with variance $\sigma_j^2 = k_B T / k_j$ at $T = 300$ K. Mirror points were constructed by inversion to $-\mathbf{Q}$, with labels assigned by Aug₂ or Aug₃.

III. RESULTS AND DISCUSSION

The results are organized in two parts, covering first exact label symmetries on hydrogen atomic orbital densities and then approximate label symmetries on the water potential energy surface.

A. Exact symmetries

We use hydrogen atomic orbital densities to demonstrate the effect of continuous and discrete label symmetries, enforced throughout by input transformation. Training points are drawn uniformly in the sphere volume of appropriate radius, and density values are normalized to $[0, 1]$ by dividing by the maximum.

1. Continuous symmetries

Our first demonstration uses the hydrogen s -orbital densities $\rho_n(r) \propto R_{n0}(r)^2$, where R_{n0} is the radial wavefunction with principal quantum number n . The label symmetry of the target is $O(3)$ invariance, or invariance under all rotations of the sphere. We enforce this symmetry by performing the regression on the rotation-invariant coordinate $r = \sqrt{x^2 + y^2 + z^2}$. For $n = 1, 2, 3$, we compare direct KRR models trained on normalized Cartesian coordinates (x, y, z) to a symmetry-adapted model trained on r alone.

Learning curves for the $1s$ orbital are shown in Fig. 2(b); results for the $2s$ and $3s$ orbitals are qualitatively similar and are presented in the Supporting Information. The dominant effect is a change in learning rate, with slopes of -0.94 , -0.93 , and -0.84 in the direct models versus -1.29 , -1.41 , and -1.32 in the radial models for $n = 1, 2, 3$, respectively. Using r as input results in a consistent slope gain factor of 1.4–1.6 across all three targets, despite differences in functional form and nodal structure. The change in slope can be attributed to dimensionality reduction rather than any feature of the specific orbitals, qualitatively matching the prediction of the effect of continuous symmetries in Ref. [28].

The same dimensionality-reduction mechanism underlies the slope improvements seen in $SE(3)$ -equivariant molecular architectures. The distinction is that the $O(3)$ symmetry exploited here is a property of the orbital-density target itself rather than of the physical space it occupies.

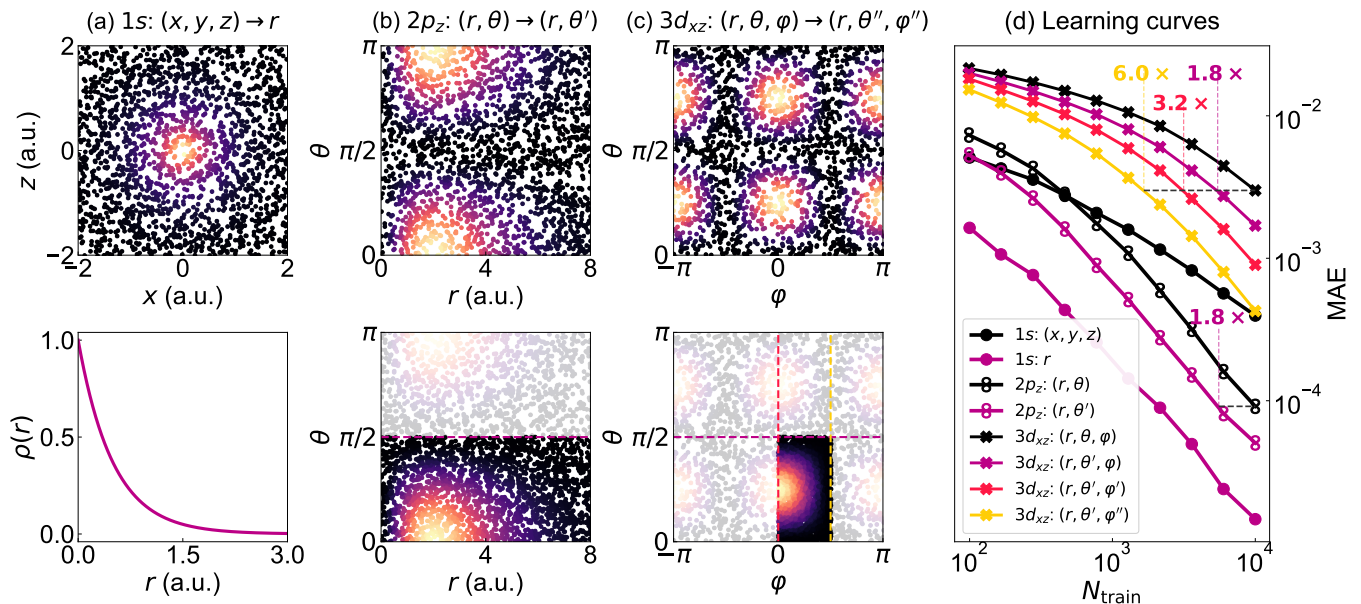


FIG. 2. Incorporation of label symmetry in hydrogen orbital densities. Dashed lines indicate symmetry planes; faded points mark the redundant domain after folding. (a) $1s$ density xz cross-section at $y = 0$ (top) and as a function of r (bottom), illustrating reduction from three Cartesian coordinates to one radial coordinate by $O(3)$ symmetry. (c) $2p_z$ density in the xz plane before (top) and after (bottom) enforcing the \mathbb{Z}_2 reflection $\theta \mapsto \theta'$. (d) $3d_{xz}$ density in (θ, φ) coordinates before (top) and after (bottom) applying all three \mathbb{Z}_2 reflections. (e) Learning curves for the $1s$, $2p_z$ and $3d_{xz}$ densities under successive symmetry operations. Dashed annotations indicate the data-efficiency gain relative to the direct models at $N_{\text{train}} = 10000$ for the $2p_z$ and $3d_{xz}$ densities.

2. Discrete symmetries

We next consider discrete point group symmetries in the densities of the $2p_z$ and $3d_{xz}$ hydrogen orbitals.

The $2p_z$ density has $D_{\infty h}$ symmetry. The continuous C_∞ subgroup accounts for the independence of the density from the azimuthal angle φ , motivating coordinates (r, θ) from the outset. The remaining discrete symmetry is the reflection σ_h through the xy plane. Enforcing it replaces θ with $\theta' = \min(\theta, \pi - \theta)$, reducing the θ domain from $[0, \pi]$ to $[0, \pi/2]$ (Fig. 2(c)). Because spherical coordinates separate, the fold in θ is independent of r .

The $3d_{xz}$ density belongs to the lower-order D_{2h} point group. Any point is part of an eight-point orbit related by three \mathbb{Z}_2 reflections across the xy , xz , and yz planes. We enforce these symmetries by defining coordinates $\theta' = \min(\theta, \pi - \theta)$, $\varphi' = |\varphi|$, and $\varphi'' = \min(|\varphi|, \pi - |\varphi|)$, which sequentially reduce the domains of θ and φ (Fig. 2(d)).

The $2p_z$ learning curves (Fig. 2(e)) exhibit two nearly parallel lines in log-log space, with fitted power-law slopes of -1.24 for the (r, θ) model and -1.20 for the (r, θ') model. The data efficiency is $1.8\times$ higher at $N = 10000$, close to the twofold reduction in the domain caused by the \mathbb{Z}_2 reflection. For $3d_{xz}$, the models are not yet in the fully asymptotic regime across the range studied. However, the cumulative data efficiency gain at $N = 10000$ is $1.8\times$, $3.2\times$, and $6.0\times$, corresponding to a per-reflection gain between 1.73 – 1.90 . The near-constant gain per reflection suggests that they act nearly independently,

meaning the total improvement compounds multiplicatively with the number of symmetries. Whether such independence holds in general depends on the coupling structure of the target. The hydrogen orbital densities factorize by construction, so each reflection acts on a fully decoupled coordinate. For a target that does not separate in the folded coordinates, successive folds would share degrees of freedom and the total gain is expected to fall short of a full factor of $|G|$.

These results establish that when the symmetry is exact, each discrete fold contributes approximately a factor of two to the effective training set size. The following section examines how this picture changes when the symmetry holds only approximately.

B. Approximate symmetries

Here we investigate the impact of approximate symmetries on ML model performance on the PES of water using data augmentation, first along individual modes in one dimension and then across the full three-dimensional PES.

1. 1D normal-mode scans

We apply label symmetry augmentation to the three vibrational normal modes of water, whose potential en-

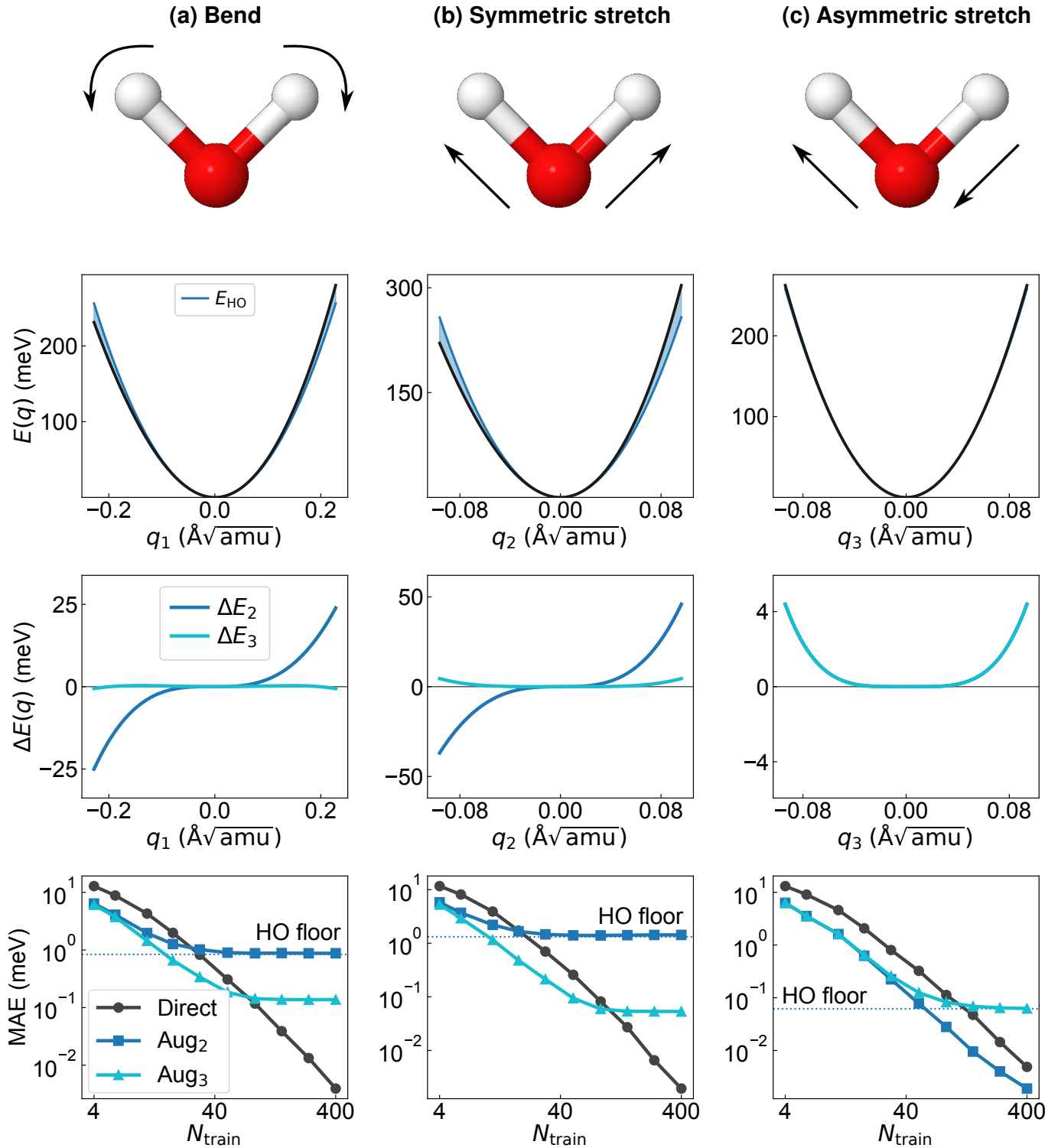


FIG. 3. Energy learning curves along the three vibrational normal modes of water: the bend (1), symmetric stretch (2), and asymmetric stretch (3). *Top row*: Schematic of each normal-mode displacement. *Second row*: Potential energy $E(q)$ (black) and harmonic reference E_{HO} (blue dashed) along the mass-weighted normal coordinate q_i . The shaded blue region denotes the anharmonicity of $E(q)$. *Third row*: The residual of the energy ΔE_n after removal of terms in the Taylor expansion up to n -th order. *Bottom row*: MAE versus N_{train} for direct training (black circles), symmetric augmentation Aug_2 (blue squares), and corrected augmentation Aug_3 (cyan triangles). The grey dotted line marks the harmonic-oscillator anharmonicity floor $\epsilon_{\infty}^{\text{HO}}$.

TABLE I. Asymptotic error floors for the three water normal-mode scans, read as plateau MAEs from Fig. 3. $\epsilon_{\infty}^{\text{HO}}$ is the baseline set by the harmonic-oscillator reference labels; $\epsilon_{\infty}^{\text{Aug}_2}$ and $\epsilon_{\infty}^{\text{Aug}_3}$ are the floors under symmetric and corrected augmentation respectively.

Mode	$\epsilon_{\infty}^{\text{HO}}$ (meV)	$\epsilon_{\infty}^{\text{Aug}_2}$ (meV)	$\epsilon_{\infty}^{\text{Aug}_3}$ (meV)
Bend	0.84	0.88	0.14
Sym. str.	1.32	1.43	0.053
Asym. str.	0.062	≤ 0.002	0.063

ergy $E(q)$ is approximately \mathbb{Z}_2 symmetric under $q \mapsto -q$. Each training point $(q_i, E(q_i))$ is augmented with a mirror point at $-q_i$, with labels assigned by either Aug₂ or Aug₃. The middle row of Fig. 3 shows the decomposition of the anharmonic residual $\Delta E = E(q) - E_{\text{HO}}(q)$ into its even and odd components for each mode, which determines the dominant convergence floor according to Eqs. (17) and (19).

Across all modes, the qualitative effect of the symmetry is a constant log-log offset in the power-law regime before approaching the error floor set by the augmentation scheme, in agreement with Eq. (7). The two symmetry-adapted learning curves provide the same performance gain at small N , diverging only once they approach their respective convergence floors. This illustrates that, in the data-starved regime, higher-order anharmonic errors are unresolved by the model, and that even a second-order harmonic estimate of the mirror label yields substantial gains whenever training data are limited.

For the bend (a), ΔE is dominated by its odd component with a smaller but nonzero even contribution. Per Eq. (17), the Aug₂ floor is set by the odd anharmonic component; correspondingly, $\epsilon_{\infty}^{\text{sym}} \approx 0.88$ meV is close to the HO error of 0.84 meV, since both are dominated by the same cubic term in ΔE . Aug₃ suppresses the odd contribution, and its floor is instead governed by the even component per Eq. (19), giving $\epsilon_{\infty}^{\text{corr}} \approx 0.14$ meV.

The symmetric stretch (b) is dominated by odd anharmonicity: positive displacements elongate both O–H bonds and are energetically softer than equivalent compressions, yielding a large cubic coefficient. The Aug₂ floor (≈ 1.43 meV) accordingly sits close to the HO baseline (1.32 meV), as both are governed by the same cubic term in ΔE . Aug₃ eliminates the leading cubic label error, and the learning curve converges to a floor more than an order of magnitude smaller (≈ 0.053 meV), consistent with the subdominant quartic anharmonicity predicted by Eq. (19). This floor is finite because, while the Hessian correction cancels the cubic contribution exactly, the residual quartic anharmonicity of the O–H stretch remains.

The asymmetric stretch (c) is qualitatively distinct because the symmetry responsible for its even parity is not an approximate geometric property of the potential but a consequence of nuclear permutation symmetry. Dis-

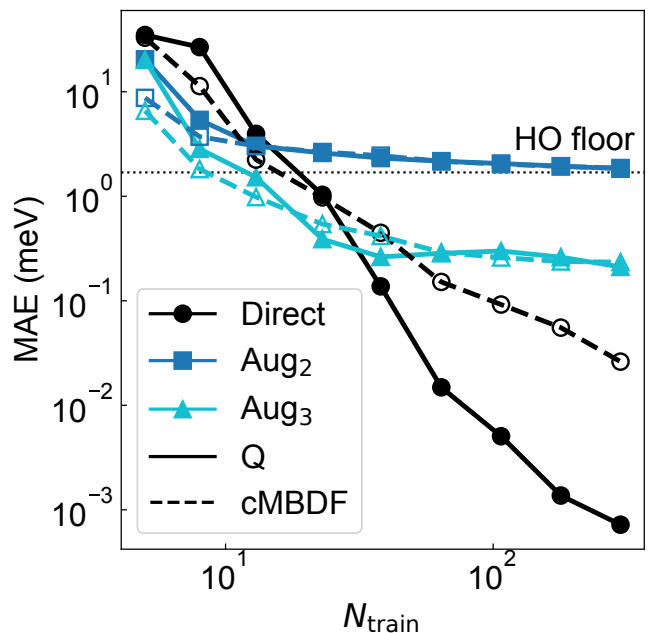


FIG. 4. Learning curves for the 3D water PES sampled at $T = 300$ K. Solid lines: normal-mode coordinate \mathbf{Q} ; dashed lines with open markers: cMBDF. Colors denote the training strategy: direct (dark), Aug₂ (blue), Aug₃ (cyan), as in Fig. 3. Grey dotted line: HO baseline (1.69 meV).

placing along this mode by $+q$ elongates one O–H bond while compressing the other; the displacement at $-q$ exchanges the roles of the two bonds. Since water’s two hydrogen atoms are identical, this exchange is a permutation of indistinguishable nuclei, and such a permutation cannot alter the Born–Oppenheimer energy. The potential $E(q)$ is therefore exactly even, $E(-q) = E(q)$, and all odd-order Taylor coefficients about $q = 0$ vanish identically. This is the same invariance enforced by permutationally invariant polynomials (PIPs) [9], which build nuclear-permutation symmetry directly into the basis functions. Aug₂ consequently assigns exact mirror labels, and the corresponding learning curve declines monotonically. Aug₃ applies a Hessian correction to an already-exact label, introducing an error proportional to $-2\Delta E(q)$ at each mirror point. When $E(-q) = E(q)$ exactly, the two labels at q average to $E_{\text{HO}}(q)$, so the asymptotic predictor is exactly E_{HO} and the floor equals the HO baseline (≈ 0.062 meV). The Aug₃ floors of the symmetric and asymmetric stretches are comparable in magnitude (0.053 and 0.063 meV, respectively), but they have distinct physical origins. In the symmetric stretch, the floor reflects a subdominant quartic term that survives after the dominant cubic is cancelled, whereas in the asymmetric stretch the quartic term is itself the leading anharmonicity.

2. Full 3D sampling

We confirm that the floor predictions of Sec. IID carry over to the full three-dimensional PES of water, sampled under the approximate inversion symmetry $\mathbf{Q} \mapsto -\mathbf{Q}$. Results for two representations, \mathbf{Q} and cMBDF, are shown in Fig. 4.

The central result is that the learning curves for both representations plateau at the same floor under each augmentation scheme. With Aug₂, both representations converge to the HO baseline (1.69 meV), consistent with Eq. (22). Aug₃ surpasses the HO baseline and converges at an error about an order of magnitude lower.

A qualitative difference from the 1D case is that the two augmented learning curves separate already at small N , whereas in one dimension they track each other until each approaches its floor. We attribute this earlier separation to the sparser coverage of mirrored regions in the effective kernel metric. In the 1D scans, training displacements are drawn from the full symmetric interval $[-q_{\max}, q_{\max}]$, so independently sampled direct points populate both sides of the equilibrium. A mirror point $-q_i$ is therefore likely to have nearby direct points with correct labels, which can partially counterweight the biased Aug₂ label in the local KRR interpolation. In three dimensions, the mirror $-\mathbf{Q}_i$ of a typical training point falls in a region that is less densely covered by independently sampled direct points at small N ; nearest-neighbor distances decrease as $N^{-1/3}$ in 3D rather than N^{-1} in 1D. The prediction near such mirrored samples is then more strongly regularized by the assigned augmented label, making the lower label error of Aug₃ visible before the asymptotic floor is reached.

Because augmentation operates entirely in Cartesian coordinate space, it is compatible with any representation that faithfully encodes molecular geometry, as confirmed by the identical floors observed for both \mathbf{Q} and cMBDF. Each local minimum of a more complex molecule requires one frequency calculation to supply the normal modes, and the convergence floors of Sec. IID apply locally, determined by the anharmonicity about that conformer.

IV. CONCLUSION

We have examined label symmetry as an inductive bias for kernel ridge regression in both exact and approximate settings. Exact symmetries are illustrated for the hydrogen atomic orbital densities which reproduce the expected learning-curve behavior: continuous $O(3)$ invariance of the s -orbital density increases the convergence rate by reducing the effective input dimensionality from three to one, while the discrete \mathbb{Z}_2^K reflection symmetries of the p_z and d_{xz} densities shift the learning-curve pre-factor without altering the slope, with each fold contributing approximately a factor of two to the effective training set size.

Approximate reflection symmetries have been illustrated for the water potential energy surface. Second order augmentations introduce an irreducible floor set by odd anharmonicity. A Hessian-based corrected mirror label, $\tilde{E}^{\text{corr}}(-\mathbf{q}) = 2E_{\text{HO}}(\mathbf{q}) - E(\mathbf{q})$, cancels the leading cubic error and shifts the floor to quartic order. Normal-mode scans confirm these predictions across modes with different odd/even anharmonic character. Augmentation up to third order requires only the equilibrium geometry, normal-mode directions, and force constants — as obtained from standard frequency analysis; i.e. no additional electronic-structure labels are needed.

The advantage of augmentation is concentrated in data-limited regimes. Chemical space has higher dimensionality than the PES of a single molecule, implying worse learning rates and the a longer-persisting data efficiency advantage over N_{train} . Quantifying the cost-accuracy trade-off of using Hessians for improved data augmentation across chemical space remains a natural direction for future work.

ACKNOWLEDGMENTS

We acknowledge the support of the Natural Sciences and Engineering Research Council of Canada (NSERC), [funding reference number RGPIN-2023-04853]. Cette recherche a été financée par le Conseil de recherches en sciences naturelles et en génie du Canada (CRSNG), [numéro de référence RGPIN-2023-04853]. This research was undertaken thanks in part to funding provided to the University of Toronto’s Acceleration Consortium from the Canada First Research Excellence Fund, grant number: CFREF-2022-00042. O.A.v.L. has received support as the Ed Clark Chair of Advanced Materials and as a Canada CIFAR AI Chair.

[1] M. Rupp, A. Tkatchenko, K.-R. Müller, and O. A. von Lilienfeld, Fast and accurate modeling of molecular atomization energies with machine learning, *Phys. Rev. Lett.* **108**, 058301 (2012).

[2] O. A. von Lilienfeld, Quantum machine learning in chemical compound space, *Angewandte Chemie International Edition* **57**, 4164 (2018), <http://dx.doi.org/10.1002/anie.201709686>.

- [3] F. A. Faber, L. Hutchison, B. Huang, J. Gilmer, S. S. Schoenholz, G. E. Dahl, O. Vinyals, S. Kearnes, P. F. Riley, and O. A. Von Lilienfeld, Prediction errors of molecular machine learning models lower than hybrid dft error, *Journal of chemical theory and computation* **13**, 5255 (2017).
- [4] B. Huang and O. A. von Lilienfeld, Quantum machine learning using atom-in-molecule-based fragments selected on the fly, *Nature chemistry* **12**, 945 (2020).
- [5] I. Batatia, P. Benner, Y. Chiang, A. M. Elena, D. P. Kovács, J. Riebesell, X. R. Advincula, M. Asta, M. Avaylon, W. J. Baldwin, *et al.*, A foundation model for atomistic materials chemistry, *The Journal of chemical physics* **163** (2025).
- [6] K. Li, B. DeCost, K. Choudhary, M. Greenwood, and J. Hattrick-Simpers, A critical examination of robustness and generalizability of machine learning prediction of materials properties, *npj Computational Materials* **9**, 55 (2023).
- [7] J. Behler and M. Parrinello, Generalized neural-network representation of high-dimensional potential-energy surfaces, *Phys. Rev. Lett.* **98**, 146401 (2007).
- [8] J. Behler, Atom-centered symmetry functions for constructing high-dimensional neural networks potentials, *J. Comp. Phys.* **134**, 074106 (2011).
- [9] B. J. Braams and J. M. Bowman, Permutationally invariant potential energy surfaces in high dimensionality, *International Reviews in Physical Chemistry* **28**, 577 (2009).
- [10] A. P. Bartók, R. Kondor, and G. Csányi, On representing chemical environments, *Phys. Rev. B* **87**, 184115 (2013).
- [11] R. Drautz, Atomic cluster expansion for accurate and transferable interatomic potentials, *Physical Review B* **99**, 014104 (2019).
- [12] A. S. Christensen, L. Bratholm, F. A. Faber, and O. A. von Lilienfeld, FCHL revisited: Faster and more accurate quantum machine learning, *The Journal of Chemical Physics* **152**, 044107 (2020).
- [13] K. T. Schütt, H. E. Sauceda, P.-J. Kindermans, A. Tkatchenko, and K.-R. Müller, Schnet—a deep learning architecture for molecules and materials, *The Journal of Chemical Physics* **148**, 241722 (2018).
- [14] M. Haghightlari, J. Li, X. Guan, O. Zhang, A. Das, C. J. Stein, F. Heidar-Zadeh, M. Liu, M. Head-Gordon, L. Bertels, *et al.*, Newtonnet: a newtonian message passing network for deep learning of interatomic potentials and forces, *Digital Discovery* **1**, 333 (2022).
- [15] V. G. Satorras, E. Hoogeboom, and M. Welling, E (n) equivariant graph neural networks, in *International conference on machine learning* (PMLR, 2021) pp. 9323–9332.
- [16] K. Schütt, O. Unke, and M. Gastegger, Equivariant message passing for the prediction of tensorial properties and molecular spectra, in *International conference on machine learning* (PMLR, 2021) pp. 9377–9388.
- [17] S. Batzner, A. Musaelian, L. Sun, M. Geiger, J. P. Mailoa, M. Kornbluth, N. Molinari, T. E. Smidt, and B. Kozinsky, E (3)-equivariant graph neural networks for data-efficient and accurate interatomic potentials, *Nature communications* **13**, 2453 (2022).
- [18] I. Batatia, D. P. Kovacs, G. Simm, C. Ortner, and G. Csányi, Mace: Higher order equivariant message passing neural networks for fast and accurate force fields, *Advances in neural information processing systems* **35**, 11423 (2022).
- [19] A. Krizhevsky, I. Sutskever, and G. E. Hinton, Imagenet classification with deep convolutional neural networks, *Advances in neural information processing systems* **25** (2012).
- [20] C. Shorten and T. M. Khoshgoftaar, A survey on image data augmentation for deep learning, *Journal of big data* **6**, 1 (2019).
- [21] T. Dao, A. Gu, A. Ratner, V. Smith, C. De Sa, and C. Ré, A kernel theory of modern data augmentation, in *International conference on machine learning* (PMLR, 2019) pp. 1528–1537.
- [22] S. Chen, E. Dobriban, and J. H. Lee, A group-theoretic framework for data augmentation, *Journal of Machine Learning Research* **21**, 1 (2020).
- [23] K. Ngo and S. Ravanbakhsh, Scaling laws and symmetry: Evidence from neural force fields, *arXiv preprint arXiv:2510.09768* (2025).
- [24] B. Tahmasebi and M. Weber, Achieving approximate symmetry is exponentially easier than exact symmetry, in *International Conference on Learning Representations* (2026) *arXiv:2512.11855*.
- [25] M. F. Langer, S. N. Pozdnyakov, and M. Ceriotti, Probing the effects of broken symmetries in machine learning, *Machine Learning: Science and Technology* **5**, 045058 (2024).
- [26] M. Domina, J. W. Abbott, P. Pegolo, F. Bigi, and M. Ceriotti, How unconstrained machine-learning models learn physical symmetries, *arXiv preprint arXiv:2603.24638* (2026).
- [27] B. Elesedy and S. Zaidi, Provably strict generalisation benefit for invariant models, in *Proceedings of the 38th International Conference on Machine Learning* (PMLR, 2021) pp. 2951–2959.
- [28] B. Tahmasebi and S. Jegelka, The exact sample complexity gain from invariances for kernel regression, in *Advances in Neural Information Processing Systems*, Vol. 36 (2023).
- [29] K.-R. Müller, S. Mika, G. Rätsch, K. Tsuda, and B. Schölkopf, An introduction to kernel-based learning algorithms, *IEEE Transactions on Neural Networks* **12**, 181 (2001).
- [30] B. Huang and O. A. von Lilienfeld, Ab initio machine learning in chemical compound space, *Chemical Reviews* **121**, 10001 (2021).
- [31] A. Blumer, A. Ehrenfeucht, D. Haussler, and M. K. Warmuth, Learnability and the Vapnik–Chervonenkis dimension, *Journal of the ACM* **36**, 929 (1989).
- [32] A. Ehrenfeucht, D. Haussler, M. Kearns, and L. Valiant, A general lower bound on the number of examples needed for learning, *Information and Computation* **82**, 247 (1989).
- [33] E. B. Baum and D. Haussler, What size net gives valid generalization?, *Advances in Neural Information Processing Systems* **1** (1988).
- [34] D. Haussler and M. Opper, *Calculation of the learning curve of Bayes optimal classification algorithm for learning a perceptron with noise* (University of California at Santa Cruz, 1991).
- [35] E. Levin, N. Tishby, and S. A. Solla, A statistical approach to learning and generalization in layered neural networks, *Proceedings of the IEEE* **78**, 1568 (1990).
- [36] H. S. Seung, H. Sompolinsky, and N. Tishby, Statistical mechanics of learning from examples, *Physical Review A*

- 45**, 6056 (1992).
- [37] J. Rissanen, Stochastic complexity and modeling, *The Annals of Statistics* **14**, 1080 (1986).
- [38] S.-i. Amari, N. Fujita, and S. Shinomoto, Four types of learning curves, *Neural Computation* **4**, 605 (1992).
- [39] S.-i. Amari, A universal theorem on learning curves, *Neural Networks* **6**, 161 (1993).
- [40] C. Cortes, L. D. Jackel, S. A. Solla, V. Vapnik, and J. S. Denker, Learning curves: Asymptotic values and rate of convergence, in *Advances in Neural Information Processing Systems*, Vol. 6 (1993) pp. 327–334.
- [41] K.-R. Müller, M. Finke, N. Murata, K. Schulten, and S.-i. Amari, A numerical study on learning curves in stochastic multilayer feedforward networks, *Neural Computation* **8**, 1085 (1996).
- [42] J. Hestness, S. Narang, N. Ardalani, G. Diamos, H. Jun, H. Kianinejad, M. M. A. Patwary, Y. Yang, and Y. Zhou, Deep learning scaling is predictable, empirically, arXiv preprint arXiv:1712.00409 (2017).
- [43] S. Spigler, M. Geiger, S. d’Ascoli, L. Sagun, G. Biroli, and M. Wyart, Asymptotic learning curves of kernel methods: Empirical data versus teacher–student paradigm, *Journal of Statistical Mechanics: Theory and Experiment* **2020**, 124001 (2020).
- [44] Z. Li, W. J. Zhang, and Q. Lin, On the asymptotic learning curves of kernel ridge regression under power-law decay, in *Advances in Neural Information Processing Systems*, Vol. 36 (2023).
- [45] S.-i. Amari and N. Murata, Statistical theory of learning curves under entropic loss criterion, *Neural Computation* **5**, 140 (1993).
- [46] J. S. Rosenfeld, A. Rosenfeld, Y. Belinkov, and N. Shavit, A constructive prediction of the generalization error across scales, in *International Conference on Learning Representations (ICLR, 2020)*.
- [47] L. Verlet, Computer “experiments” on classical fluids. I. Thermodynamical properties of Lennard-Jones molecules, *Physical Review* **159**, 98 (1967).
- [48] Q. Sun, T. C. Berkelbach, N. S. Blunt, G. H. Booth, S. Guo, Z. Li, J. Liu, J. D. McClain, E. R. Sayfutyarova, S. Sharma, S. Wouters, and G. K.-L. Chan, PySCF: the Python-based simulations of chemistry framework (2017).
- [49] J.-D. Chai and M. Head-Gordon, Long-range corrected hybrid density functionals with damped atom–atom dispersion corrections, *Physical Chemistry Chemical Physics* **10**, 6615 (2008).
- [50] S. Grimme, J. Antony, S. Ehrlich, and H. Krieg, A consistent and accurate ab initio parametrization of density functional dispersion correction (DFT-D) for the 94 elements H-Pu, *Journal of Chemical Physics* **132**, 154104 (2010).
- [51] F. Weigend and R. Ahlrichs, Balanced basis sets of split valence, triple zeta valence and quadruple zeta valence quality for H to Rn: Design and assessment of accuracy, *Physical Chemistry Chemical Physics* **7**, 3297 (2005).
- [52] S. Heinen, D. Khan, and O. A. von Lilienfeld, QML2: Quantum machine learning package (2024), software package.
- [53] D. Khan, S. Heinen, and O. A. von Lilienfeld, Quantum machine learning at record speed: Many-body distribution functionals as compact representations, arXiv preprint arXiv:2303.16312 (2023).
- [54] D. Khan, S. Heinen, and O. A. von Lilienfeld, Generalized convolutional many-body distribution functional representations, *Proceedings of the National Academy of Sciences* **122**, e2415662122 (2025).